Supplementary materials

Appendix Table 1. Anisotropic displacement parameters (Å^2) for Mg and O in both the single-site and split-site hydrogen models, with $U_{11} = U_{22}$ and $U_{13} = U_{23} = 0$ for each atom.

		$Mg(OH)_{1.78}F_{0.22}$	$Mg(OH)_{1.16}F_{0.84}$	$Mg(OH)_{1.99}F_{0.01}$
		single-site hydrogen model		
Mg	U_{11}:	0.0119(6)	0.0112(6)	0.0104(3)
	U_{33}:	0.0405(10)	0.0371(11)	0.0237(5)
	U_{12}:	0.0059(3)	0.0056(3)	0.0052(2)
	U_{eq}:	0.0214(6)	0.0198(6)	0.0148(3)
O	U_{11}:	0.0135(7)	0.0119(8)	0.0125(4)
	U_{33}:	0.0312(11)	0.0222(12)	0.0202(6)
	U_{12}:	0.0067(3)	0.0059(4)	0.0063(2)
	U_{eq}:	0.0194(6)	0.0153(6)	0.0151(3)
		three-site split-atom hydrogen model		
Mg	U_{11}:	0.0119(6)	0.0112(6)	0.0103(3)
	U_{33}:	0.0404(10)	0.0371(11)	0.0237(5)
	U_{12}:	0.0059(3)	0.0056(4)	0.00516(17)
	U_{eq}:	0.0214(6)	0.0198(6)	0.0148(2)
O	U_{11}:	0.0134(7)	0.0119(8)	0.0125(4)
	U_{33}:	0.0312(11)	0.0223(12)	0.0203(6)
	U_{12}:	0.0059(3)	0.0059(4)	0.00625(19)
	U_{eq}:	0.0193(6)	0.0153(6)	0.0151(3)

Appendix Table 2. The temperature dependence of the OH-stretching modes in the synthetic and natural brucite samples.

$Mg(OH)_{1.78}F_{0.22}$*		$Mg(OH)_{1.16}F_{0.84}$*		$Mg(OH)_{1.99}F_{0.01}$#	
v_i (cm^{-1})	$(\partial v_i/\partial T)_p$ ($cm^{-1}\cdot K^{-1}$)	v_i (cm^{-1})	$(\partial v_i/\partial T)_p$ ($cm^{-1}\cdot K^{-1}$)	v_i (cm^{-1})	$(\partial v_i/\partial T)_p$ ($cm^{-1}\cdot K^{-1}$)
Raman-active					
3647	-0.0109(7)	3641	-0.0106(5)	3650	-0.0167(6)
IR-active					
3804	-0.0083(16)	3804	-0.0182(14)	——	——
3697	-0.0301(6)	3695	-0.0427(8)	3702	-0.0267(6)
3660	-0.0226(9)	3660	-0.0314(7)	——	——
3645	-0.0103(5)	3644	-0.0182(6)	——	——
3513	0.0176(19)	3513	0.034(2)	——	——

*: this study; #: Zhu et al. (2019).

Appendix Table 3. The pressure dependence of the vibrational frequencies for both Raman-active and IR-active OH-stretching modes measured in this study.

$Mg(OH)_{1.78}F_{0.22}$		$Mg(OH)_{1.16}F_{0.84}$		$Mg(OH)_{1.99}F_{0.01}$	
ν_i (cm^{-1})	$(\partial\nu_i/\partial P)_T$ ($cm^{-1}\cdot GPa^{-1}$)	ν_i (cm^{-1})	$(\partial\nu_i/\partial P)_T$ ($cm^{-1}\cdot GPa^{-1}$)	ν_i (cm^{-1})	$(\partial\nu_i/\partial P)_T$ ($cm^{-1}\cdot GPa^{-1}$)
Raman-active					
3646	-4.329(9)	3641	-3.853(8)	3651	-6.977(8)
——	——	3670[a]	-2.214(14)	——	——
IR-active					
3804	-5.818(21)	3804	-4.915(17)	——	——
3695	2.482(6)	3691	2.173(11)	3703	-0.217(9)
3660	-1.517(7)	3660	-1.476(9)	——	——
3645	-4.136(12)	3645	-3.425(10)	3638[b]	-8.667(18)
3513	-8.15(3)	3513	-7.05(3)	——	——

a: measured at P = 8.4 GPa; *b*: measured at P = 4.5 GPa.

Figure S1

Fig. S1 Microphotograph of a recovered sample piece ($Mg(OH)_{1.16}F_{0.84}$) after the high-*P,T* experiment.

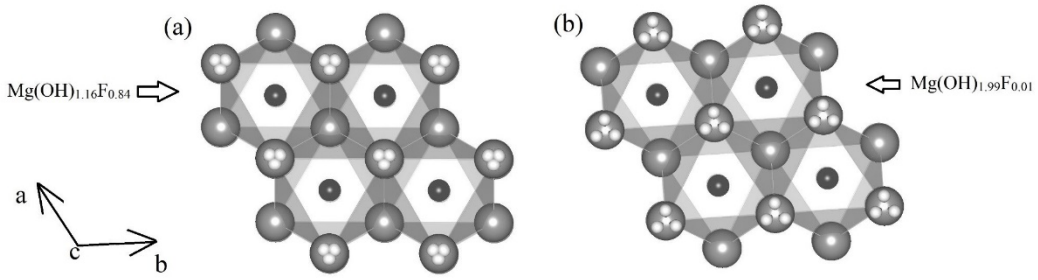

Figure S2

Fig. S2 Illustration of fluorine effect on the three-site split-atom hydrogen model between **(a)** $Mg(OH)_{1.16}F_{0.84}$ and (b) $Mg(OH)_{1.99}F_{0.01}$. The local structures are viewed along the ***c*** direction. The large balls on the corners and medium balls at the centers of octahedra present O^{2-} and Mg^{2+} ions, respectively. Only protons (small balls) on the upper side of the MO6-octahedra layer are present, while substituted F^- anions are not shown in the figure for simplification.

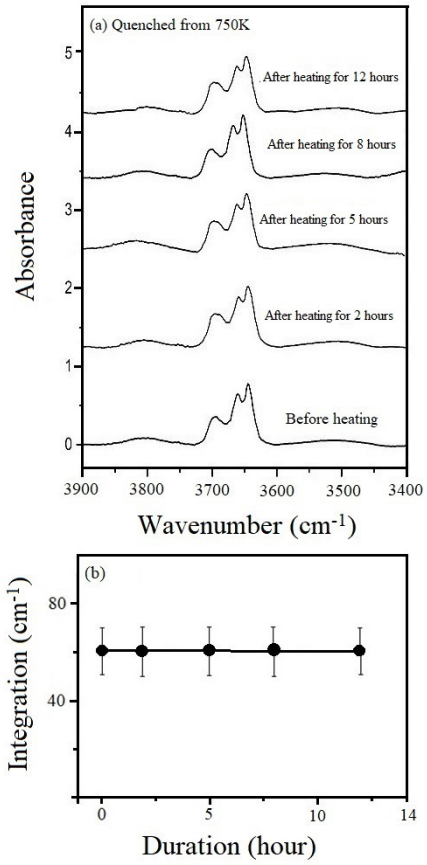

Figure S3

Fig. S3 (a) The quenched FTIR spectra for Mg(OH)1.78F0.22 after heating for various durations at 750 K, and the one before heating is also compared at the bottom. **(b)** Integrations of IR-active signals for the OH-stretching modes in the range from 3400 to 3900 cm^{-1}, which is plotted as a function of heating duration. The linear regression for these data points is almost parallel to the horizontal axis.